

# Analyzing local exciton generation profiles as a means to extract transport lengths in organic solar cells

John R. Tumbleston,<sup>1</sup> Doo-Hyun Ko,<sup>2</sup> Edward T. Samulski,<sup>2</sup> and Rene Lopez<sup>1,\*</sup>

<sup>1</sup>*Department of Physics and Astronomy, University of North Carolina at Chapel Hill, Phillips Hall, CB 3255, Chapel Hill, North Carolina 27599, USA*

<sup>2</sup>*Department of Chemistry, Caudill and Kenan Laboratories, University of North Carolina at Chapel Hill, CB 3290, Chapel Hill, North Carolina 27599, USA*

(Received 10 September 2010; revised manuscript received 29 October 2010; published 19 November 2010)

In this work, we determine the carrier-transport lengths of electrons and holes ( $L_{e,h}$ ) for bulk heterojunction (BHJ) organic solar cells using a method applicable to functional devices. By linking the local exciton generation profile [ $G(x)$ ] in the photoactive layer to photocurrent losses, we are able to determine the onset of bimolecular recombination, which is the dominant loss process of free carrier transport. Even though many factors affect photocurrent generation, we single out bimolecular recombination by measuring the scaling of photocurrent with light intensity as a function of applied voltage. For the common BHJ system, annealed poly-3-hexylthiophene:[6,6]-phenyl-C61-butyric acid methyl ester (P3HT:PCBM), a minimum for  $L_e$  in PCBM is found to be 340 nm while  $L_h$  is estimated to be 90 nm for P3HT. The relationship between  $G(x)$  and carrier transport is further exemplified by demonstrating a scaling exponent below that for traditional space-charge-limited photocurrent. Likewise, by incorporating a drift/diffusion model, an intuitive link between  $G(x)$  and charge transport is established where recombination is shown to occur in regions of the photoactive layer far from the electrode of the slowest carrier species. Finally, the consequences of  $L_{e,h}$  on device design for operation under 1 Sun conditions are described.

DOI: [10.1103/PhysRevB.82.205325](https://doi.org/10.1103/PhysRevB.82.205325)

PACS number(s): 73.50.Pz, 72.20.Jv, 88.40.jr

## I. INTRODUCTION

Significant improvement in the performance of bulk heterojunction (BHJ) organic solar cells has occurred over the past few years with efficiencies over 8%.<sup>1</sup> Advances in device performance have been accompanied in part by greater characterization of electron and hole transport. Free carrier transport in the photoactive layer occurs after a number of physical processes including (1) exciton photogeneration in the donor, (2) exciton diffusion to the donor/acceptor interface, (3) creation of a charge-transfer state, and (4) exciton dissociation into free carriers. Unlike bilayer devices where free carriers are created at a single donor/acceptor interface, free carriers in BHJ solar cells are created throughout the bulk due to the continuous network of donor/acceptor interfaces. Because light is absorbed throughout the active layer, a distribution of lengths exists that carriers must travel in order to be extracted.

Due to the strong internal electric fields in BHJ devices, electron and hole transport has been traditionally characterized in terms of electron and hole drift lengths

$$L_{e,h} = \mu_{e,h} \tau_{e,h} E, \quad (1)$$

where  $\mu_{e,h}$  is the carrier mobility,  $\tau_{e,h}$  is the carrier lifetime, and  $E$  is the internal electric field. Usually,  $\mu_{e,h}$  is the desired quantity and can be measured under steady state with space-charge-limited current (SCLC) (Ref. 2) and field effect transistor<sup>3,4</sup> techniques. The low-mobility values determined from these methods compared to inorganic semiconductors has led to the belief that active-layer thicknesses must be kept around 100 nm in order to reduce transport losses.<sup>5,6</sup> Given the different device geometries and measurement conditions for these methods,  $\mu_{e,h}$  can span orders of magnitude

depending on the technique due to its dependence on carrier density,<sup>7</sup> polymer chain orientation,<sup>8</sup> and whether or not the donor and acceptor are mixed or in pure phases.<sup>3,9</sup> In particular, for the standard BHJ material system, poly-3-hexylthiophene:[6,6]-phenyl-C61-butyric acid methyl ester (P3HT:PCBM), both  $\mu_e > \mu_h$  (Ref. 9) and  $\mu_e < \mu_h$  (Refs. 3 and 10) have been observed. Because these results depend on the technique and are conducted without illumination, it is difficult to guarantee that the derived transport lengths will appropriately describe the charge transport of photogenerated carriers in a working device. Contact barriers also play a critical role for methods like SCLC where carriers are injected,<sup>11</sup> which could be more effectively avoided by measuring photogenerated current that is extracted from the device.<sup>12</sup> While various transient techniques also exist that monitor the dynamics of charge transport,<sup>13</sup> they can be more complex and intricate to implement than steady-state measurements. Therefore, a simple steady-state method would be advantageous to determine  $L_{e,h}$  for photogenerated carriers in a working device under standard operating conditions.

Herein, we propose a method to extract  $L_{e,h}$  for solar cells under illumination. We demonstrate the method for P3HT:PCBM in order to compare our results with other transport measurements for this donor:acceptor system. By measuring the scaling of the photocurrent with light intensity over a range of applied voltages for different local exciton generation profiles [ $G(x)$ ], we measure  $L_h=90$  nm in P3HT and determine  $L_e > 340$  nm in PCBM under standard annealing and preparation conditions. Electron and hole transport are probed independently by measuring both standard and inverted devices. Furthermore, a scaling exponent below that for the traditional space-charge-limited photocurrent (i.e., 0.75) is observed due to the dependence of charge transport

on  $G(x)$ . Our analysis is supported with an electro-optical model, which elucidates regions in the photoactive layer where free carrier loss occurs. Finally, our results help guide active-layer thickness restrictions under standard 1 Sun operating conditions.

## II. EXPERIMENT

In order to compare transport of electrons and holes, both standard and inverted solar cells were fabricated. Cleaned ITO-coated (150 nm;  $\rho=5 \times 10^{-4} \Omega \text{ cm}$ ) glass substrates were coated with either PEDOT:PSS (55 nm; Baytron PH500) or sol-gel  $\text{TiO}_x$  (Ref. 6) for standard and inverted devices, respectively. Standard device substrates were annealed in air at 140 C for 10 min while inverted substrates were heated in an oven at 450 C for 60 min to convert  $\text{TiO}_x$  to anatase  $\text{TiO}_2$  (20 nm). Next, solutions of either P3HT (15 or 30 mg/mL) and PCBM (12 or 24 mg/mL) in a 1:0.8 ratio in chlorobenzene were spin coated at speeds ranging from 500 to 1300 rpm to achieve desired active-layer thicknesses ( $t$ ) between 80 and 390 nm. Finally, either Al (90 nm) or  $\text{WO}_3/\text{Ag}$  (10 nm/90 nm) were thermally evaporated as the back contact (12  $\text{mm}^2$  active area) for standard and inverted devices, respectively. Standard devices were annealed at 145 C for 10 min after evaporation while inverted devices received the same thermal treatment prior to electrode deposition.

Measurement under 1 Sun conditions was conducted in the glovebox while the photocurrent under high incident angle ( $65^\circ$ ) was measured in air using a blue laser ( $\lambda=473 \text{ nm}$ ). The photocurrent from the laser along with the incident light intensity ( $P_{\text{light}}$ ) was measured simultaneously via a beam splitter on the optical setup. No degradation occurred during device measurement time ( $<3 \text{ hr/device}$ ). Furthermore, significant reflection losses from the air/glass substrate interface were avoided by placing the glass substrate (side opposite active layer) in contact with a half-cylinder and index matching oil. This configuration prevented the incident beam from bending toward normal due to refraction in the glass substrate.

In spite of the differing electrodes, electron/hole transporting layer materials, and thermal treatment of ITO, both inverted and standard devices have similar performance under 1 Sun conditions for devices with  $t=130 \text{ nm}$  (thicker active layers will be discussed below). Short-circuit currents ( $J_{sc}$ ) of 10.4  $\text{mA/cm}^2$  and 9.2  $\text{mA/cm}^2$ , open-circuit voltages ( $V_{oc}$ ) of 0.57 V and 0.60 V, fill factors (FFs) of 53% and 51%, efficiencies of 3.1% and 2.8%, series resistances (inverse slope at 0.75 V) of 8.8  $\Omega \text{ cm}^2$  and 9.3  $\Omega \text{ cm}^2$ , and shunt resistances (inverse slope of dark current at 0.0 V) of 0.4  $\text{M}\Omega \text{ cm}^2$  and 0.5  $\text{M}\Omega \text{ cm}^2$  were achieved for inverted and standard devices, respectively. Furthermore, atomic force microscopy of the top surface of P3HT:PCBM spincast on both  $\text{TiO}_2$  and PEDOT:PSS showed insignificant differences in film morphology.<sup>14</sup> Based on these results, we assume that changes in carrier transport in P3HT:PCBM related to morphology differences due to choice of electron/hole transporting layers are minimal compared to modification of the transport based on  $G(x)$ .

In this work, we determine  $G(x)$  ( $x$  dependence dropped and implied for remainder of this work) in the photoactive layer through an optical modeling scheme that has been used for both standard<sup>15,16</sup> and inverted devices.<sup>10,17,18</sup> Optical modeling is based on the transfer/scattering matrix method<sup>19</sup> and is checked against a commercial software package (DIFRACTMOD from RSoft Design Group). Optical properties of each material layer are determined via spectroscopic ellipsometry,<sup>14</sup> which closely match reported values.<sup>15,20</sup> Layer thicknesses are measured with cross-section scanning electron microscopy and verified with profilometry and by fitting simulations of the spectral reflection to the measured reflection by varying layer thicknesses.<sup>21</sup>

To model electrical performance,  $G$  is used as input in a drift/diffusion effective medium model of the active layer with Ohmic contacts<sup>22</sup> implemented in COMSOL MULTIPHYSICS. This metal/insulator/metal picture is a simplification of the studied devices where the transporting layers are disregarded along with any Schottky barriers. However, the similar  $V_{oc}$  and series resistance for each device type indicates contacts that are comparable in function. Furthermore, the inclusion of slight barriers should not significantly affect carrier extraction especially for voltages below maximum power point where the conclusions from this work are drawn.<sup>23</sup> Besides  $G$ , other parameters in the electrical model are taken from literature for P3HT:PCBM (Ref. 9) including  $\mu_e(2.0 \times 10^{-7} \text{ m}^2/\text{V s})$ ,  $\mu_h(1.0 \times 10^{-8} \text{ m}^2/\text{V s})$ , relative dielectric constant (3.4), electron/hole pair separation distance (1.8 nm), exciton decay rate ( $2.0 \times 10^4 \text{ s}^{-1}$ ), and effective density of states ( $2.5 \times 10^{25} \text{ m}^{-3}$ ).<sup>14</sup> The parameter that dictates  $V_{oc}$  in the model, the effective band gap (0.95 eV), is fit to the experimental data. Finally, the modified form of Langevin bimolecular recombination<sup>24</sup> is used to explicitly relate loss of carriers during transit to the slowest carrier species.

## III. RESULTS AND DISCUSSION

### A. Exciton generation profile sets required transport distances

Even though multiple steps occur between exciton generation and carrier transport, we assume that the profile of free carrier generation essentially matches that of exciton generation due to the short ( $<20 \text{ nm}$ ) (Refs. 25 and 26) diffusion length of photoexcited excitons to the donor/acceptor interface. Figure 1 shows  $G$  for both inverted and standard solar cells with  $t=390 \text{ nm}$  and  $P_{\text{light}}=10.0 \text{ mW/cm}^2$  and  $10.9 \text{ mW/cm}^2$ , respectively. Due to the high angle ( $65^\circ$ ) and relatively short excitation wavelength ( $\lambda=473 \text{ nm}$ ), an exponentially decreasing  $G$  profile is set up in the photoactive layer. Under these conditions,  $G$  drops by 3 orders of magnitude from one side of the active layer to the other for both devices. This type of profile is very different from those under normal incidence for thinner active layers that vary by an order of magnitude where the maximum is centered in the middle of the active layer.<sup>16,18,27</sup> In this study, monotonically decreasing profiles are guaranteed even for thinner active layers due to the chosen incident angle and wavelength.

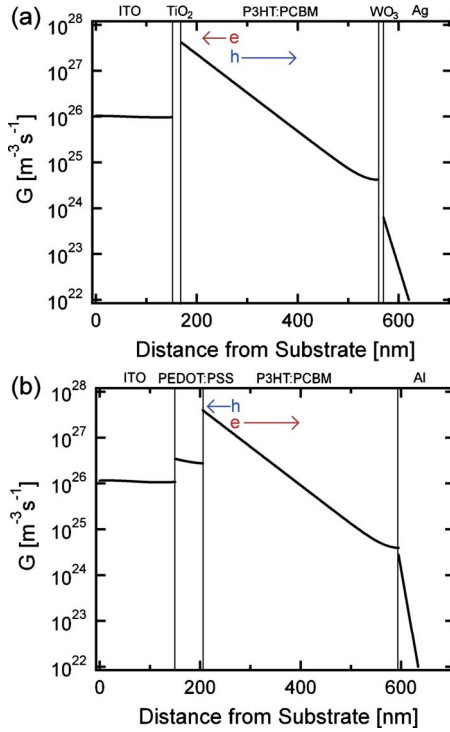


FIG. 1. (Color online) Local exciton generation profile ( $G$ ) for (a) inverted and (b) standard device architectures with active-layer thicknesses of 390 nm under  $10.0 \text{ mW/cm}^2$  and  $10.9 \text{ mW/cm}^2$   $\lambda=473 \text{ nm}$  ( $p$ -polarized) incident light intensity, respectively, at  $65^\circ$  incidence.  $G$  represents the generation rate of excitons in the active layer while it signifies parasitic absorption losses in all other materials. It is determined from an optical model and sets the average required transport distance for electrons and holes in the active layer depending on the device type. Arrows indicate the direction of electron and hole transport where the average hole is required to travel much further than the average electron for the inverted device. The opposite is true for the standard device.

As shown in Fig. 1, the average hole has a much longer distance to travel than the average electron for the inverted device. The opposite is true for the standard solar cell. In this way, we are able to set the average required transport distance for electrons and holes ( $D_{e,h}$ ) simply by choosing inverted or standard devices with specific  $t$ . For example,  $D_e$  is defined for inverted devices by weighting  $G$  by the distance ( $x$ ) to the cathode

$$D_e = \frac{\int_0^t (G)(x)dx}{\int_0^t (G)dx}. \quad (2)$$

$D_h$  is then given by  $t - D_e$  where similar expressions are used to determine  $D_{e,h}$  for standard devices. The incident wavelength essentially sets  $D_{e,h}$ , where  $D_h=310 \text{ nm}$  and  $230 \text{ nm}$  for  $\lambda=473 \text{ nm}$  and  $600 \text{ nm}$ , respectively, under normal incidence for the inverted device with  $t=390 \text{ nm}$ . By increasing the incident angle to  $65^\circ$ ,  $D_h$  is lengthened to  $340 \text{ nm}$  and  $250 \text{ nm}$  for these wavelengths, respectively. Herein, we use a

high angle ( $65^\circ$ ) and relatively short excitation wavelength ( $\lambda=473 \text{ nm}$ ) to set up the longest possible values of  $D_{e,h}$  for each  $t$ .<sup>14</sup> In this work,  $D_h$  is varied from  $340 \text{ nm}$  for inverted solar cells with  $t=390 \text{ nm}$  down to  $40 \text{ nm}$  for standard devices with  $t=130 \text{ nm}$ . A similar range is obtained for  $D_e$ . It should be noted that the incident light polarization also affects  $G$  under non-normal incidence but has a negligible effect on  $D_{e,h}$  values compared to the differences obtained by varying  $t$ . All work presented here is for  $p$ -polarized illumination as nearly identical results were obtained under  $s$  polarization.

## B. Photocurrent scaling with light intensity

Determining if  $D_{e,h}$  set by  $G$  are too far for electrons or holes to travel is done by measuring the photocurrent ( $J_{photo} = |J_{light} - J_{dark}|$ ) over a range of light intensities ( $P_{light}$ ) and fitting to a power-law relationship. Because  $J_{photo}$  describes the current output solely due to photogeneration, the effects of series and shunt resistance that modify electrical performance under illumination are removed.<sup>28</sup> However, high series resistance can affect the power-law scaling of  $J_{photo}$ ,<sup>29</sup> but values measured herein range between  $5$  and  $35 \text{ } \Omega \text{ cm}^2$ , which are not high enough to have a significant impact.

Figure 2 shows  $J_{photo}$  under various  $P_{light}$  for both device types with  $t=390 \text{ nm}$ .  $J_{photo}$  is given over a range of reverse and forward applied voltages ( $V_{app}$ ) up to  $V_{oc}$  where the conclusions of this work are drawn from voltages below maximum power point and into the reverse bias regime. It is clear that the shapes of the curves are very different for inverted and standard solar cells. For example, the inverted device requires high reverse-bias application ( $V_{app} = -5 \text{ V}$ ) in order to reach the saturated photocurrent ( $J_{sat}$ ) under the highest  $P_{light}$  while the standard device nearly saturates at short circuit.

The cause of the different behaviors for inverted and standard devices can be further understood by determining the power-law scaling of the photocurrent with light intensity ( $P_{light}$ )

$$J_{photo} = \beta (P_{light})^\alpha, \quad (3)$$

where  $\beta$  is a constant. By varying  $P_{light}$ , bimolecular recombination can be triggered due to its dependence on the product of electron and hole concentration.<sup>30</sup> Because this is the loss process of free carriers, linearity of  $\alpha$  indicates the unrestricted, lossless transport of carriers to the electrodes. In this way, bimolecular recombination can be separated from other loss processes that reduce  $J_{photo}$  below  $J_{sat}$  and also depend on  $V_{app}$ , such as the electric field dependence of exciton dissociation.<sup>31</sup> Even though exciton dissociation also depends on  $V_{app}$ , it is monomolecular in nature and is accompanied by a linear scaling of  $J_{photo}$  with  $P_{light}$ . It should be noted that we do not distinguish between bimolecular and other higher order recombination processes.<sup>32</sup> We simply interpret a nonlinear scaling of  $J_{photo}$  with  $P_{light}$  to indicate loss of free carriers during transit where we label this loss as bimolecular recombination. Also, the dependence of  $\alpha$  on carrier density indicates that the number of free carriers must

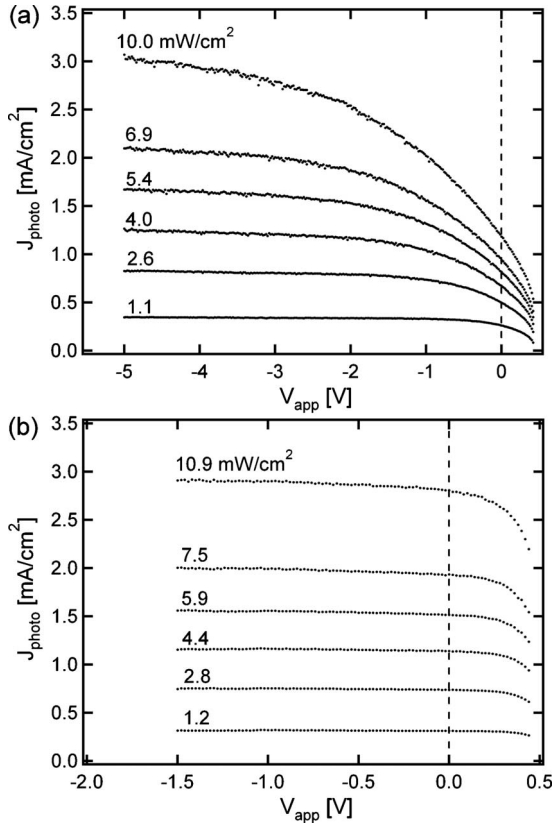


FIG. 2. Photocurrent ( $J_{photo} = |J_{light} - J_{dark}|$ ) over a range of applied voltages ( $V_{app}$ ) for (a) inverted and (b) standard device architectures with active-layer thicknesses of 390 nm under a range of  $\lambda = 473$  nm laser-light intensities ( $P_{light}$ ) and  $65^\circ$  incidence. The inverted device requires high reverse bias in order for  $J_{photo}$  to reach the saturated photocurrent for the highest  $P_{light}$ . Conversely,  $J_{photo}$  for the standard device nearly saturates at short circuit.

be similar for all devices in order to make accurate comparisons between the various device configurations. This is confirmed from similar  $J_{sat}$  values (Fig. 2) and from the optical model that indicates that the photoactive layer absorbs between 77% and 90% of the incident light for both standard and inverted devices regardless of  $t$ . Furthermore,  $J_{sat}$  under the maximum  $P_{light}$  from the laser is between 1/4 and 1/3 of the measured  $J_{sat}$  under 1 Sun conditions. This sets the effective maximum sun-equivalent intensity of the laser to be between 1/4 and 1/3 Sun.

While  $\alpha$  is usually only cited at short circuit,<sup>28,33</sup> it is determined here at each  $V_{app}$  to show clear nonlinear and linear regimes. Values are given in Fig. 3 for both inverted and standard devices with different active-layer thicknesses ( $80 \leq t \leq 390$  nm). It is observed for inverted devices that increasing  $t$  causes  $\alpha$  to deviate from unity for greater reverse bias application (i.e., higher internal electric fields). On the other hand, for standard devices with  $t = 130$  and 390 nm,  $\alpha$  remains close to unity over the entire voltage range. Under these illumination conditions with monotonically decreasing  $G$ , inverted devices suffer from recombination due to limited free carrier transport while standard devices do not.

The contrasting transport between standard and inverted devices indicates that hole transport is limited for

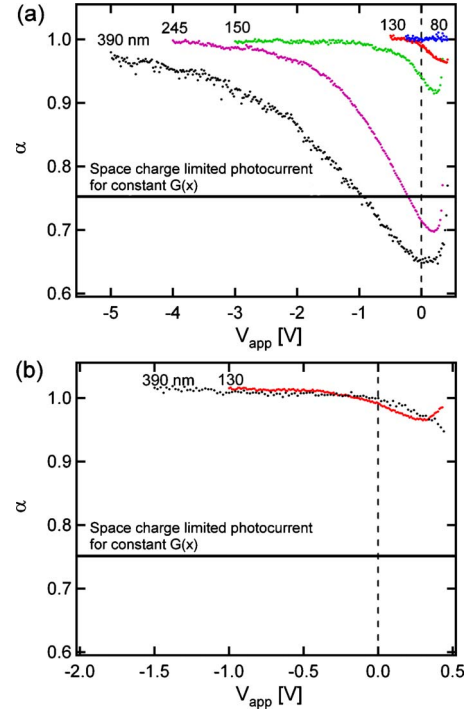


FIG. 3. (Color online) Scaling factors ( $\alpha$ ) when the photocurrent is fit to a power law,  $J_{photo} = \beta(P_{light})^\alpha$  for (a) inverted and (b) standard device architectures with various active-layer thicknesses ( $t$ ) under  $\lambda = 473$  nm illumination and  $65^\circ$  incidence. Nonlinearities are observed at higher reverse bias as  $t$  is increased for inverted devices while both thicknesses of standard devices show linear scaling. The case of space-charge-limited photocurrent for constant  $G$  ( $\alpha = 0.75$ ) is also shown for reference.

P3HT:PCBM under the prescribed preparation conditions for thicker values of  $t$ . For the thickest inverted solar cell ( $t = 390$  nm),  $D_h = 340$  nm while  $D_e = 50$  nm. A large negative  $V_{app}$  (i.e., high electric field) is required to achieve  $\alpha = 1.0$  where all the carriers are forced out of the active layer without recombining. However, as  $t$  is reduced, the  $V_{app}$  where  $\alpha = 1.0$  moves toward the forward bias regime. For the  $t = 130$  nm device, slight nonlinearity is only observed near maximum power point, which means that  $L_h > D_h$  even for the low electric fields that approach open-circuit conditions.  $D_h = 90$  nm for the  $t = 130$  nm device, so it is determined that  $L_h = 90$  nm for P3HT. Conversely,  $D_e$  is probed for the standard devices, where transport is not limited for even the largest  $t$  as  $\alpha$  remains close to unity even up to maximum power point. For the  $t = 390$  nm device  $D_e = 340$  nm, which is not long enough overcome  $L_e$ . Therefore, we set a lower limit of  $L_e > 340$  nm in PCBM for the annealed P3HT:PCBM system.

Another equally important observation from Fig. 3 are  $\alpha$  values below 0.75 for the inverted devices with  $t = 245$  and 390 nm. It has been shown for solar cells where  $\mu_e$  and  $\mu_h$  differ by two orders of magnitude, space-charge-limited photocurrent occurs with  $\alpha = 0.75$ .<sup>34</sup> However, this lower limit of  $\alpha$  is achieved if  $G$  can be approximated as constant in the active layer. For the  $t = 390$  nm inverted device,  $G$  varies by 3 orders of magnitude [Fig. 1(a)]. This imposes the average hole to travel much further ( $D_h = 340$  nm) than under a con-

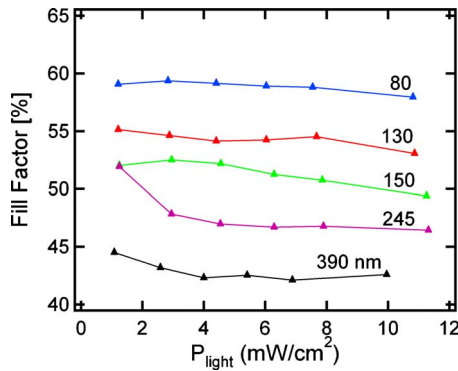


FIG. 4. (Color online) FF for inverted devices with varying active-layer thickness ( $t$ ) as measured from the data for Fig. 3(a). The FF for standard devices (not shown) is similar to that of the  $t = 80$  nm inverted device indicating that the longer transport distance set by the exciton generation profile for thicker photoactive layers can greatly reduce the FF.

stant generation profile ( $D_h = t/2 = 195$  nm). Thus, there appears to be a significant impact of  $G$  on  $\alpha$  reaching values at or below 0.75. This signifies that severely unbalanced transport and space-charge-limited photocurrent can be strongly influenced by  $G$  along with  $\mu_{e,h}$  values. In terms of the scaling of  $J_{photo}$  with  $V_{app}$  a power dependence of 0.45 for  $-2.0 \leq V_{app} \leq 0$  is determined for the inverted device under highest  $P_{light}$ . This type of voltage scaling is also indicative of space-charge-limiting behavior, especially when observed under reverse bias away from open circuit. No such behavior is observed for the standard devices.

Finally, the effect of bimolecular recombination on inverted device performance is also observed in device FF. Figure 4 shows the FF for light intensities used to determine  $\alpha$  from Fig. 3. It is evident that as  $t$  increases, the FF drops accordingly. For standard devices (not shown), the FF values are similar to those for the  $t = 80$  nm inverted device. Because serial resistance is similar for all devices and monomolecular recombination only plays a minor role as observed above, we attribute the reduction in FF with thicker  $t$  to enhancement in bimolecular recombination due to the increase in  $D_h$  imposed by  $G$ .

### C. Interplay between local exciton generation and recombination

While the macroscopic description of charge transport is given by measurement of  $L_{e,h}$ , further insight can be gained with a model that describes the local profile of recombination in P3HT:PCBM. While various models have been proposed that assume identical carrier transport between electrons and holes,<sup>35,36</sup> the drift/diffusion model allows for unbalanced charge transport and nonconstant  $G$ .<sup>22</sup> In this model, transport is described using  $\mu_{e,h}$ , where we set  $\mu_e = 20\mu_h$  (Ref. 9) given our result that  $L_e > L_h$ . It should also be noted that we take  $\mu_{e,h}$  to be constant throughout the active layer to reflect our bulk measurements of  $L_{e,h}$  even though charge transport can vary on the microscale for BHJ solar cells.<sup>37</sup>

Figure 5 shows the measured current density under illumination ( $J_{light}$ ) for the inverted and standard devices with

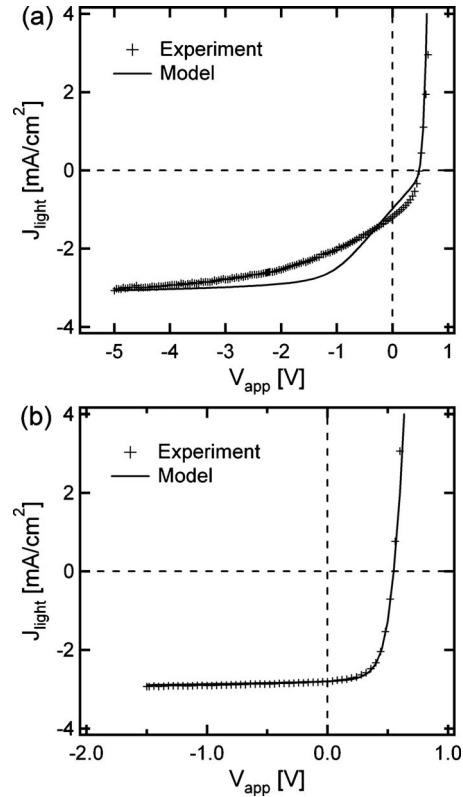


FIG. 5. Experimental and modeled current density under illumination ( $J_{light}$ ) vs applied voltage ( $V_{app}$ ) for (a) inverted and (b) standard devices with active-layer thicknesses of 390 nm under the illumination conditions for Fig. 1. Simulations are generated by inputting  $G$  from Fig. 1 in the drift/diffusion model of the active layer with an electron and hole mobility ( $\mu_{e,h}$ ) mismatch ( $\mu_e = 20\mu_h$ ) to represent the shorter hole than electron-transport length ( $L_e > L_h$ ).

$t = 390$  nm under laser illumination with  $P_{light} = 10.0$  mW/cm<sup>2</sup> and 10.9 mW/cm<sup>2</sup>, respectively. When the generation profiles of Fig. 1 are input in the model keeping all other parameters constant, very different behavior is predicted for standard and inverted devices. Compared to the standard device, the inverted solar cell has a much lower  $J_{sc}$  and FF, which matches the trends of the experimental data. Saturation of  $J_{light}$  is also observed to occur under high reverse-bias conditions while it saturates near short circuit for the standard solar cell. The saturation voltages of  $J_{light}$  also qualitatively match those for both  $J_{photo}$  and  $\alpha$  of Figs. 2 and 3, respectively.

The utility of the model can now be realized by calculating the net generation rate ( $U$ ) (Ref. 22) of free carriers for both inverted and standard devices at short circuit ( $t = 390$  nm). Figure 6(a) shows that for the inverted device  $U$  is reduced near the cathode by orders of magnitude due to bimolecular recombination. This ultimately leads to a reduction in photocurrent extraction (Fig. 4) because the majority of the slower carrier species (i.e., holes) need to transport much further than  $L_h$  resulting in a buildup of space charge and reduction in the internal field near the cathode. On the other hand, for the standard device,  $U$  essentially matches  $G$  of Fig. 1 which indicates minimal recombination. Even

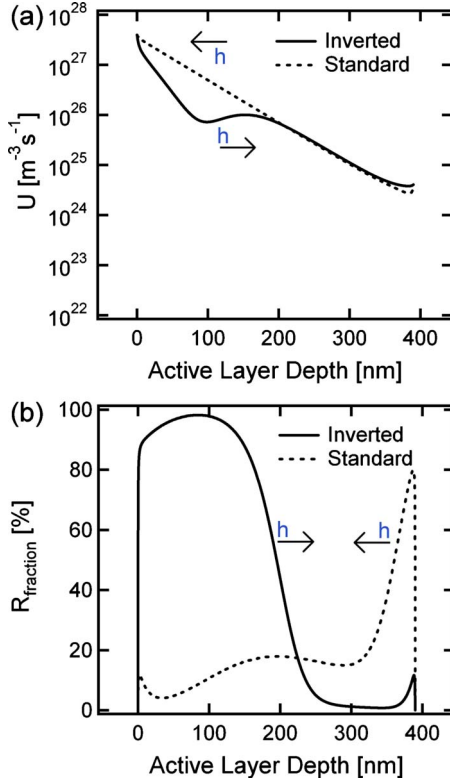


FIG. 6. (Color online) (a) Net generation rate ( $U$ ) and (b) fraction of carriers that undergo bimolecular recombination ( $R_{fraction}$ ) at short circuit for both inverted and standard devices with active-layer thicknesses of 390 nm as modeled in Fig. 5. Arrows indicate opposite direction of hole transport for inverted and standard solar cells.

though the active layer is very thick, high extracted current is achieved because both  $D_h < L_h$  and  $D_e < L_e$  are satisfied for the standard device.

This intuitive picture is further exemplified by calculating the fraction of carriers that undergo bimolecular recombination  $R_{fraction}$  for both devices [Fig. 6(b)]. It is noted that the strength of recombination is more significant in areas of the active layer where holes have a further distance to travel. This is especially true for the inverted device where most of the carriers are created far from the anode as set by  $G$  [Fig. 6(b)]. However, even for the standard device where few carriers are created far from the anode [Fig. 1(b)], there is still significant recombination in this region of the active layer.

#### D. Implications for 1 Sun operation

Even though the nonconstant  $G$  profiles [Fig. 1] in this work are useful in determining  $L_e$  and  $L_h$ , they are different from the generation profiles under 1 Sun conditions at normal incidence. In this section, device performance using the exact 1 Sun  $G$  and average value of the 1 Sun exciton generation rate ( $\langle G \rangle$ ) are modeled and compared for both standard and inverted solar cells as a function of  $t$ . Figure 7 shows the ratio of  $J_{sc}$  values predicted from the model using  $G$  compared to those using  $\langle G \rangle$  under 1 Sun illumination and normal incidence. It should be noted that  $G$  is determined for

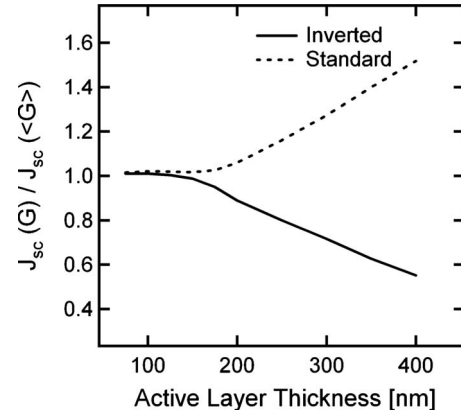


FIG. 7. Ratio of short-circuit current ( $J_{sc}$ ) using exact exciton generation profile under 1 Sun illumination and normal incidence ( $G$ ) compared to the average profile ( $\langle G \rangle$ ) for inverted and standard devices as a function of active-layer thickness.

1 Sun illumination by integrating all  $G$  profiles over the spectral range where P3HT:PCBM absorbs light ( $350 \leq \lambda \leq 675$ ) using the wavelength-dependent light intensities from the AM (air mass) 1.5 spectrum. It is clear that up to  $t = 180$  nm, there is little difference in  $J_{sc}$ , which indicates minimal recombination losses. However, as the active layer is increased,  $J_{sc}$  computed from  $G$  is larger than that using  $\langle G \rangle$  for standard devices. This occurs because  $\langle G \rangle$  creates more holes further from the anode causing an increase in recombination and drop in output current. The opposite is true for the inverted devices where use of  $G$  results in a smaller  $J_{sc}$  compared to use of  $\langle G \rangle$ . For this case,  $\langle G \rangle$  creates more holes closer to the anode and effectively assists hole transport. This result agrees well with our previous determination of  $L_{e,h}$  where a device thickness above  $2L_h$  begins to show significant signs of recombination losses. However, for standard devices,  $t$  can be increased beyond  $2L_h$  due to the nonconstant  $G$  that creates more carriers closer to the anode, which ultimately assists hole transport.

In terms of 1 Sun performance, this work supports that of others who have shown high performance for standard P3HT:PCBM solar cells with  $t \geq 350$  nm.<sup>33,38</sup> For active layers of this thickness,  $L_e > L_h$  actually assists device performance and allows for thicker active layers to be used because carrier creation is weighted more heavily toward the anode. In our work, standard devices with  $t = 390$  nm achieved 1 Sun efficiency of 3.5%, which is higher than those with  $t = 130$  nm (2.8%). The higher efficiency is due entirely to higher  $J_{sc}$  from enhanced light absorption as  $V_{oc}$  (0.59 V) and FF (52%) are similar. On the other hand,  $L_e > L_h$  proves detrimental to thicker inverted device performance where the efficiency for  $t = 390$  nm devices remains near 1% due to reduced FF (43%) and  $J_{sc}$  (5.2 mA/cm<sup>2</sup>). However,  $\mu_e < \mu_h$  has also been observed when doctor blading the active layer from orthoxylene,<sup>10</sup> which would then assist inverted device performance by making  $L_e < L_h$ . Either way,  $L_e \neq L_h$  can actually allow for the use of thicker active layers ( $t > 200$  nm) to absorb more light without significant transport losses. This is especially true for BHJ blends like P3HT:PCBM that do not suffer from monomolecular recom-

ination losses that may become more significant as  $t$  increases.<sup>15</sup>

#### IV. CONCLUSIONS

In conclusion, we have demonstrated a simple method to extract  $L_{e,h}$  for functional solar cells by measuring the scaling of the photocurrent with light intensity over a range of applied voltages for different exciton generation profiles. For annealed P3HT:PCBM, we observe hole transport to be much more restricted than electron transport, which actually assists device performance for standard solar cells with thicker active layers. For inverted devices, transport is severely limited and results in a scaling exponent below that for the traditional space-charge-limited photocurrent with a constant generation profile. Our analysis is supported with an electro-optical model, which indicates that the slower carrier suffers significant recombination far away from its final des-

tinuation (holes from the anode in this case). Finally, these results support the premise that thicker active layers could be used to absorb more light for BHJ systems where  $L_e \neq L_h$ . It also has implications for more complicated architectures with nonplanar photoactive layers such as photonic crystal<sup>39</sup> and grating<sup>40</sup> designs where the distance carriers needs to travel can have a greater range than for planar devices. Special care needs to be taken to assess the role of carrier transport for this new generation of organic solar-cell devices.

#### ACKNOWLEDGMENTS

Special thanks are given to Abay Gadisa for stimulating conversation and useful suggestions regarding the manuscript. Support for this work is from NSF (Solar: Grant No. DMR-0934433) and UNC-Chapel Hill Institute for the Environment. Acknowledgment is also made to the donors of The American Chemical Society Petroleum Research Fund (Grant No. 49187-DNI10) for partial support of this research.

\*Corresponding author: rln@physics.unc.edu

<sup>1</sup>Solarmer Energy Inc. press release, 27 July 2010.

<sup>2</sup>V. D. Mihailetchi, L. J. A. Koster, P. W. M. Blom, C. Melzer, B. de Boer, J. K. J. van Duren, and R. A. J. Janssen, *Adv. Funct. Mater.* **15**, 795 (2005).

<sup>3</sup>M. Caironi, T. Agostinelli, D. Natali, M. Sampietro, R. Cugola, M. Catellani, and S. Luzzati, *J. Appl. Phys.* **102**, 024503 (2007).

<sup>4</sup>C. R. Newman, C. D. Frisbie, D. A. da Silva Filho, J.-L. Bredas, P. C. Ewbank, and K. R. Mann, *Chem. Mater.* **16**, 4436 (2004).

<sup>5</sup>S. H. Park, A. Roy, S. Beaupre, S. Cho, N. Coates, J. S. Moon, D. Moses, M. Leclerc, K. Lee, and A. J. Heeger, *Nat. Photonics* **3**, 297 (2009).

<sup>6</sup>J. Y. Kim, S. H. Kim, H.-H. Lee, K. Lee, W. Ma, X. Gong, and A. J. Heeger, *Adv. Mater.* **18**, 572 (2006).

<sup>7</sup>C. Tanase, E. J. Meijer, P. W. M. Blom, and D. M. de Leeuw, *Phys. Rev. Lett.* **91**, 216601 (2003).

<sup>8</sup>L. H. Jimison, M. F. Toney, I. McCulloch, M. Heeney, and A. Salleo, *Adv. Mater.* **21**, 1568 (2009).

<sup>9</sup>V. D. Mihailetchi, H. Xie, B. de Boer, L. J. A. Koster, and P. W. M. Blom, *Adv. Funct. Mater.* **16**, 699 (2006).

<sup>10</sup>T. Ameri, G. Dennler, C. Waldauf, P. Denk, K. Forberich, M. C. Scharber, C. J. Brabec, and K. Hingerl, *J. Appl. Phys.* **103**, 084506 (2008).

<sup>11</sup>R. W. I. de Boer, M. Jochemsen, T. M. Klapwijk, A. F. Morpurgo, J. Niemax, A. K. Tripathi, and J. Pflaum, *J. Appl. Phys.* **95**, 1196 (2004).

<sup>12</sup>V. D. Mihailetchi, L. J. A. Koster, and P. W. M. Blom, *Appl. Phys. Lett.* **85**, 970 (2004).

<sup>13</sup>S. Tiwari and N. C. Greenham, *Opt. Quantum Electron.* **41**, 69 (2009).

<sup>14</sup>See supplementary material at <http://link.aps.org/supplemental/10.1103/PhysRevB.82.205325> for atomic force microscopy of top surface of P3HT:PCBM, all optical properties measured via spectroscopic ellipsometry, details regarding electrical simulations, and data for normal incidence photocurrent.

<sup>15</sup>J. D. Kotlarski, P. W. M. Blom, L. J. A. Koster, M. Lenes, and L.

H. Slooff, *J. Appl. Phys.* **103**, 084502 (2008).

<sup>16</sup>A. J. Moulé, J. B. Bonekamp, and K. Meerholz, *J. Appl. Phys.* **100**, 094503 (2006).

<sup>17</sup>F.-C. Chen, J.-L. Wu, and Y. Hung, *Appl. Phys. Lett.* **96**, 193304 (2010).

<sup>18</sup>D. W. Zhao, S. T. Tan, L. Ke, P. Liu, A. K. K. Kyaw, X. W. Sun, G. Q. Lo, and D. L. Kwong, *Sol. Energy Mater. Sol. Cells* **94**, 985 (2010).

<sup>19</sup>S. G. Tikhodeev, A. L. Yablonskii, E. A. Muljarov, N. A. Gippius, and T. Ishihara, *Phys. Rev. B* **66**, 045102 (2002).

<sup>20</sup>D.-H. Ko, J. R. Tumbleston, M.-R. Ok, H. Chun, R. Lopez, and E. T. Samulski, *J. Appl. Phys.* **108**, 083101 (2010).

<sup>21</sup>G. Dennler, K. Forberich, M. C. Scharber, C. J. Brabec, I. Tomiš, K. Hingerl, and T. Fromherz, *J. Appl. Phys.* **102**, 054516 (2007).

<sup>22</sup>L. J. A. Koster, E. C. P. Smits, V. D. Mihailetchi, and P. W. M. Blom, *Phys. Rev. B* **72**, 085205 (2005).

<sup>23</sup>J.-T. Shieh, C.-H. Liu, S.-R. Tseng, Y.-C. Chao, and S.-F. Horng, *J. Appl. Phys.* **107**, 084503 (2010).

<sup>24</sup>L. J. A. Koster, V. D. Mihailetchi, and P. W. M. Blom, *Appl. Phys. Lett.* **88**, 052104 (2006).

<sup>25</sup>A. Huijser, T. J. Savenije, A. Shalav, and L. D. A. Siebbeles, *J. Appl. Phys.* **104**, 034505 (2008).

<sup>26</sup>P. E. Shaw, A. Ruseckas, and I. D. W. Samuel, *Adv. Mater.* **20**, 3516 (2008).

<sup>27</sup>J. Gilot, I. Barbu, M. M. Wienk, and R. A. J. Janssen, *Appl. Phys. Lett.* **91**, 113520 (2007).

<sup>28</sup>R. A. Marsh, C. R. McNeill, A. Abrusci, A. R. Campbell, and R. H. Friend, *Nano Lett.* **8**, 1393 (2008).

<sup>29</sup>J. R. Tumbleston, D.-H. Ko, E. T. Samulski, and R. Lopez, *J. Appl. Phys.* **108**, 084514 (2010).

<sup>30</sup>C. G. Shuttle, B. O'Regan, A. M. Ballantyne, J. Nelson, D. D. C. Bradley, and J. R. Durrant, *Phys. Rev. B* **78**, 113201 (2008).

<sup>31</sup>V. D. Mihailetchi, L. J. A. Koster, J. C. Hummelen, and P. W. M. Blom, *Phys. Rev. Lett.* **93**, 216601 (2004).

<sup>32</sup>G. Juška, K. Genevičius, N. Nekrašas, G. Šliaužys, and G. Denn-

- ler, *Appl. Phys. Lett.* **93**, 143303 (2008).
- <sup>33</sup>A. Moulé and K. Meerholz, *Appl. Phys. B: Lasers Opt.* **92**, 209 (2008).
- <sup>34</sup>V. D. Mihailetschi, J. Wildeman, and P. W. M. Blom, *Phys. Rev. Lett.* **94**, 126602 (2005).
- <sup>35</sup>M. Limpinsel, A. Wagenpfahl, M. Mingeback, C. Deibel, and V. Dyakonov, *Phys. Rev. B* **81**, 085203 (2010).
- <sup>36</sup>P. Schilinsky, C. Waldauf, J. Hauch, and C. J. Brabec, *J. Appl. Phys.* **95**, 2816 (2004).
- <sup>37</sup>L. S. C. Pingree, O. G. Reid, and D. S. Ginger, *Nano Lett.* **9**, 2946 (2009).
- <sup>38</sup>L. Zeng, C. W. Tang, and S. H. Chen, *Appl. Phys. Lett.* **97**, 053305 (2010).
- <sup>39</sup>D.-H. Ko, J. R. Tumbleston, L. Zhang, S. Williams, J. M. DeSimone, R. Lopez, and E. T. Samulski, *Nano Lett.* **9**, 2742 (2009).
- <sup>40</sup>S.-I. Na, S.-S. Kim, J. Jo, S.-H. Oh, J. Kim, and D.-Y. Kim, *Adv. Funct. Mater.* **18**, 3956 (2008).